Spectroscopic and computational investigations of Cobalt(II) binding to the innate immune protein human calprotectin

Spectroscopic and computational investigations of Cobalt(II) binding to the innate immune protein human calprotectin

Spectroscopic and Computational Investigations of Cobalt(II) Binding to the Innate Immune Protein Human Calprotectin

Michelle M. Killian[1], Megan B. Brophy[2], Elizabeth M. Nolan[2,*], and Thomas C. Brunold[1,*]

[1]*Department of Chemistry, University of Wisconsin - Madison, Madison, Wisconsin 53706*

[2]*Department of Chemistry, Massachusetts Institute of Technology, Cambridge, Massachusetts 02139*

Correspondence: brunold@chem.wisc.edu, lnolan@mit.edu

Abstract

Human calprotectin (CP) is an innate immune protein that participates in the metal-withholding response to infection by sequestering essential metal nutrients from invading microbial pathogens. CP is comprised of S100A8 (α subunit, 10.8 kDa) and S100A9 (β subunit, 13.2 kDa). Two transition-metal binding sites of CP form at the S100A8/S100A9 dimer interface. Site 1 is a His_3Asp motif comprised of His83 and His87 from the S100A8 subunit and His20 and Asp30 from the S100A9 subunit. Site 2 is an unusual hexahistidine motif composed of S100A8 residues His17 and His27 and S100A9 residues His91, His95, His103, and His105. In the present study, the His_3Asp and His_6 sites of CP were further characterized by utilizing Co^{2+} as a spectroscopic probe. Magnetic circular dichroism spectroscopy was employed in conjunction with electron paramagnetic resonance spectroscopy and density functional theory computations to characterize the Co^{2+}-bound S100A8(C42S)/S100A9(C3S) CP-Ser variant and six site variants that allowed the His_3Asp and His_6 sites to be further probed. Our results provide new insight into the metal-binding sites of CP-Ser and the effect of amino acid substitutions on the structure of site 2.

Keywords

Calprotectin, immune protein, electron paramagnetic resonance, magnetic circular dichroism, density functional theory.

Statements and Declarations

The authors declare no competing financial interest.

Introduction

Microbial pathogens employ first-row transition metals (e.g. Mn, Fe, Ni, Cu, Zn) in a variety of enzymatic processes and must acquire these inorganic cofactors from their host environment in order to replicate and cause disease.[1-4] To combat microbial invasion, the human innate immune system launches a metal-withholding response that lowers metal availability to starve the invading pathogen and inhibit its growth.[1, 4, 5] Human calprotectin (CP) is an innate immune protein that participates in the metal-withholding response to infection.[6] In the current working model, CP inhibits microbial colonization by sequestering divalent first-row transition-metal ions including Mn^{2+}, Fe^{2+}, Ni^{2+}, and Zn^{2+} in the extracellular space.[6]

As a heterooligomeric member of the S100 family of Ca^{2+}-binding proteins, CP is comprised of S100A8 (α subunit, 10.8 kDa) and S100A9 (β subunit, 13.2 kDa).[7] CP primarily exists as a αβ heterodimer or $(\alpha\beta)_2$ heterotetramer.[7-10] Each CP heterodimer harbors a total of six sites for cation binding, including four EF-hand domains for Ca^{2+} binding (two in each S100 subunit) and two sites that form at the S100A8/S100A9 interface, designated as site 1 (His_3Asp) and site 2 (His_6), that coordinate divalent first-row transition-metal ions (Figure 1).[11-16] Apo CP exists as the αβ heterodimer and Ca^{2+} binding to the EF-hands of S100A8 and S100A9 results in the self-association of two heterodimers to form the $(\alpha\beta)_2$ heterotetramer.[7-10, 17, 18] Ca^{2+}-induced tetramerization increases the transition-metal ion binding affinities of both the His_3Asp and His_6 sites of CP, enhances antimicrobial activity, and confers resistance to host proteases.[14-16, 19-21]

The two transition-metal binding sites of CP have been extensively studied.[6] Site 2 has received the most attention to date. It was first identified in the crystal structure of Ca^{2+}-bound CP-Ser (the S100A8(C42S)/S100A9(C3S) variant) as a His_4 motif composed of S100A8 residues

His17 and His27 and S100A9 residues His91 and His95.[13] However, subsequent crystallographic[11, 12] and spectroscopic[12, 20, 22] studies of Mn^{2+}-bound CP-Ser revealed that site 2 is a remarkable hexahistidine motif with His103 and His105 from the S100A9 C-terminal tail, defined as residues 96-114 of this subunit, completing an octahedral Mn^{2+} coordination sphere (Figure 2 A). Subsequently, utilization of this biologically unprecedented and highly symmetric His_6 binding motif for sequestering Fe^{2+}, Ni^{2+} and Zn^{2+} was established.[15, 16, 23] Crystal structures of CP-Ser with Mn^{2+} and Ni^{2+} bound at the His_6 site revealed that the S100A9 C-terminal tail becomes ordered with M^{2+} binding and plays an essential role in the ability of CP to sequester kinetically labile ions because it encapsulates the metal ion and excludes water molecules from the coordination site.[11, 14, 24, 25]

Site1 is a His_3Asp motif comprised of His83 and His87 from the S100A8 subunit and His20 and Asp30 from the S100A9 subunit (Figure 2B). His_3Asp motifs are present in the related S100 homodimers S100A7 and S100A12.[26-28] A crystal structure of Mn^{2+}- and Ca^{2+}- bound CP-Ser revealed electron density corresponding to a metal ion in the His_3Asp site and two possible modes of ligation, monodentate and bidentate, for Asp30 (PDB ID 4GGF[11], Figure 2 B). In addition, magnetic circular dichroism (MCD) spectroscopic studies indicated that Fe^{2+} binds to the His_3Asp site in a 5-coordinate geometry, but it remains unknown if the fifth coordination site is occupied by the second oxygen atom of the Asp30 side chain or a water-derived molecule.[29] Crystallographic studies of Ni^{2+}-bound CP-Ser in the presence and absence of Ca^{2+} ions revealed that the coordination mode of Asp30 is modulated by Ca^{2+} binding to the nearby EF-hand domains, resulting in 4-coordinate and 6-coordinate Ni^{2+} complexes in the Ca^{2+}-bound and Ca^{2+}-free forms, respectively.[14, 25] Although site 1 coordinates multiple metal ions, biological investigations demonstrated that it only sequesters Zn^{2+} and Cu^{2+} from microbes.[30-32]

One early study of CP designed to identify its metal-binding sites employed Co^{2+} as a spectroscopic probe.[19] Co^{2+} has been widely used as a spectroscopic probe of the coordination geometry of zinc proteins due to the characteristic spectra displayed by Co^{2+} in different coordination environments and the fact that zinc enzymes frequently retain both the native geometry and enzymatic activity with Co^{2+} substitution.[33-37] The prior study using Co^{2+} and employing CP-Ser variants that lacked one or both metal-binding sites established that both sites coordinate Co^{2+} and provided the first spectroscopic signatures of the His_3Asp and His_6 sites.[19] Electronic absorption spectra of the Co^{2+}-bound variants ΔHis_4 (site 2 His→Ala substitutions for the isolated study of site 1) and ΔHis_3Asp (site 1 His/Asp→Ala substitutions for the study of site 2) were consistent with 4- or 5-coordinate Co^{2+} ligation by the His_3Asp site and centrosymmetric, 6-coordinate ligation by site 2.[19]

MCD spectroscopy is a particularly sensitive tool for probing the geometric and electronic structures of transition metal ions in protein environments.[38, 39] Like absorption spectra, MCD spectra of Co^{2+}-bound small molecules and metalloproteins display characteristic patterns for different coordination geometries.[40, 41] MCD spectra of 4-coordinate, tetrahedral Co^{2+} complexes typically display an intense negative feature at lower energy along with a positive feature at slightly higher energy in the 15,600–18,000 cm^{-1} range.[40] Alternatively, MCD spectra of 5-coordinate Co^{2+} complexes are characterized by a pair of negative features in approximately the same energy range.[40] MCD spectra of synthetic 6-coordinate Co^{2+} complexes invariably display a weak negative feature centered near 20,000 cm^{-1} with intensity and shape that vary depending on the degree of distortion from an ideal octahedral geometry.[40, 42] This feature is sometimes accompanied by a second, very weak negative feature at slightly higher energy.[43, 44]

Small spectral variations in these patterns are observed for different protein environments, but the general patterns remain largely unaffected.[41]

The objective of the present study was to further characterize the two transition-metal binding sites of CP-Ser in solution. To this end, we leveraged MCD spectroscopy in conjunction with electron paramagnetic resonance (EPR) spectroscopy and density functional theory (DFT) computations to characterize Co^{2+} bound to the His_6 and His_3Asp sites of CP-Ser. Our results provide additional information about how this remarkable metal-sequestering protein interacts with divalent first-row transition metal ions.

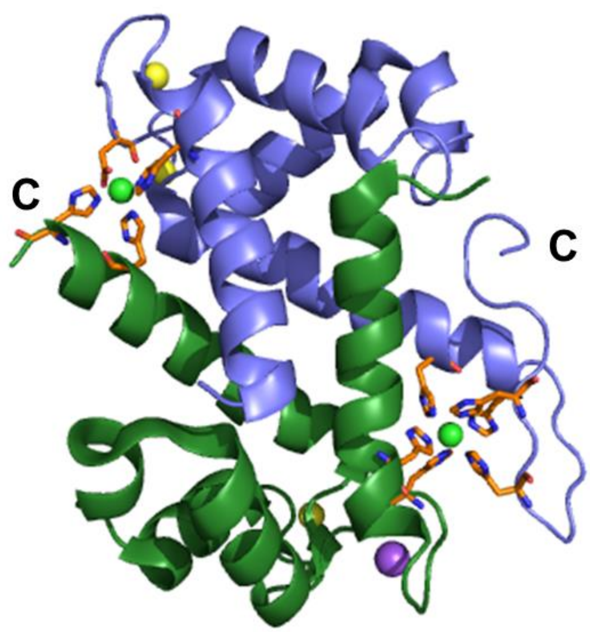

Figure 1. X-ray crystal structure of the CP $\alpha\beta$ heterodimer in the Ca^{2+}-, Na^{2+}- and Ni^{2+}-bound tetramer (PDB ID 5W1F).[14] S100A8 is shown in green, and S100A9 is shown in blue, with C-termini indicated. The Ca^{2+} ions in the canonical EF-hand loops are depicted as yellow spheres, and Na^{+} ions occupying the non-canonical loops are depicted as purple spheres. Ni^{2+}-binding residues are shown in orange, and the Ni^{2+} ions are depicted as green spheres.

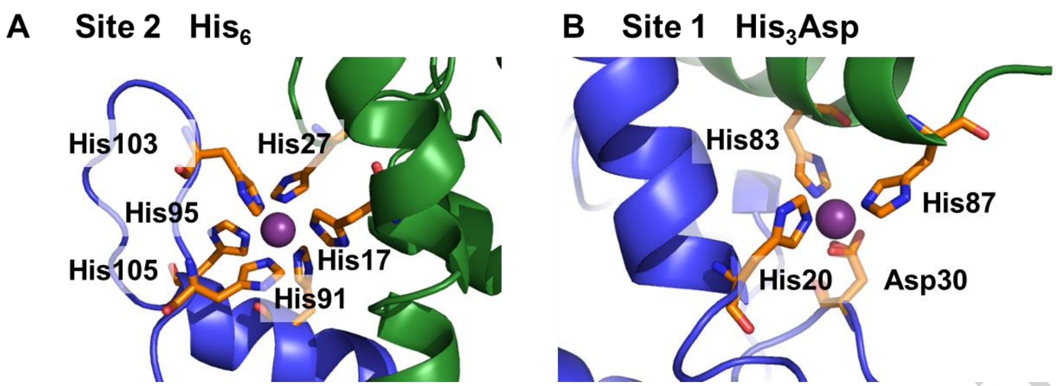

Figure 2. The transition metal-binding sites of CP observed in the X-ray crystal structure of Mn^{2+}-bound CP-Ser (PBD file 4GGF).[11] The His_6 motif with Mn^{2+} at 100% occupancy (A) and the His_3Asp motif with a metal ion presumed to be Mn^{2+} at 50% occupancy (B). S100A8 is colored green, S100A9 is colored blue, and the Mn^{2+} ions are colored purple. The residues comprising the metal-binding motifs are shown in orange.

Experimental and Computational Methods

Protein Purification. Variants of the human calprotectin S100A8 and S100A9 subunits (Table 1, Figure S1) were produced in *Escherichia coli* BL21(DE3) cells and the heterodimers were reconstituted and purified as described previously.[15, 19] All variants were purified as the apo heterodimers and stored in 20 mM HEPES, 100 mM NaCl (pH 8.0) at -80 °C. All protein concentrations, determined using calculated extinction coefficients (Table S1), are reported for the $\alpha\beta$ heterodimer, and equivalents of Co^{2+} are relative to the $\alpha\beta$ heterodimer.

The CP-Ser ΔHis_3Asp(D98A) variant was prepared and characterized using reported methods.[19] The pET41a-S100A9(C3S)(H20A)(D30A)(D98A) variant was prepared using two rounds of quick change mutagenesis starting from pET41a-S100A9(C3S)(D98A).[22] The S100A8 and S100A9 subunits were overexpressed and purified in *E. coli* BL21(DE3) cells harboring pET41a-S100A8(H83A)(H87A)[19] or pET41a-S100A9(C3S)(H20A)(D30A)(D98A), respectively, as described for CP-Ser and other CP-Ser variants (Tables S2-S3).[19] The protein was evaluated by mass spectrometry, analytical size exclusion chromatography (Figure S2 and

Table S4), and CD spectroscopy (Figure S3) as previously described for CP-Ser and other CP-Ser variants.[19]

Table 1. Differences in Amino Acid Sequences of Relevant Calprotectin Species

Protein	S100A8	S100A9	Reference
CP	Wild-type	Wild-type	[19]
CP-Ser	(C42S)	(C3S)	[19]
CP-Ser ΔHis_4	(C42S)(H17A)(H27A)	(C3S)(H91A)(H95A)	[19]
CP-Ser ΔHis_3Asp	(C42S)(H83A)(H87A)	(C3S)(H20A)(D30A)	[19]
CP-Ser ΔHis_3Asp D98A	(C42S)(H83A)(H87A)	(C3S)(H20A)(D30A)(D98A)	[45]
CP-Ser ΔHis_3Asp H103A	(C42S)(H83A)(H87A)	(C3S)(H20A)(D30A)(H103A)	[45]
CP-Ser ΔHis_3Asp H105A	(C42S)(H83A)(H87A)	(C3S)(H20A)(D30A)(H105A)	[45]
CP-Ser ΔHis_3Asp AHA	(C42S)(H83A)(H87A)	(C3S)(H20A)(D30A)(H103A)(H105A)	[45]

Magnetic Circular Dichroism Spectroscopy. Protein samples were thawed on ice and concentrated with buffer exchange by multiple (3-4) centrifugation cycles at 4 °C with ice-chilled buffer (75 mM HEPES, 100 mM NaCl, pH 7.0) using a 10 kDa Centricon filter. Final protein concentrations were verified by measuring the room-temperature electronic absorption spectra of diluted aliquots at 280 nm (heterodimer ε_{280} = 18,450 $M^{-1}cm^{-1}$) on a Varian Cary 5e spectrophotometer. Aqueous solutions of 50 mM Co^{2+} were prepared by dissolving $CoCl_2$ salt (Aldrich, 99.999%) in Milli-Q water. For each MCD sample, protein aliquots were concentrated to 2.2-2.5 mM and subsequently mixed with ~60% (v/v) ice-chilled glycerol (glassing agent) prior to the addition of ice-chilled Co^{2+} stock solution. The colorless CP-Ser and ΔHis_4 protein solutions turned pale pink and purple, respectively, upon cobalt binding, while the ΔHis_3Asp and ΔHis_3Asp variant protein solutions remained colorless in this process. The final concentration of each sample was 1.0-1.1 mM $\alpha\beta$ heterodimer, with 0.80-0.84 equivalents of Co^{2+} and 58-65% (v/v) glycerol.

Samples were injected into 2-mm pathlength MCD cells fitted with quartz windows and immediately frozen and stored in liquid nitrogen. Low-temperature (4.5 K) electronic absorption and variable temperature (4.5, 8.0, 15.0, and 25.0 K) MCD data were collected with a Jasco J-715 spectropolarimeter in conjunction with an Oxford Instruments SM-4000 8 T superconducting magnetocryostat. Contributions from the circular dichroism signal and glass strain were removed from the MCD data by taking the difference between data obtained with the magnetic field aligned parallel and antiparallel to the light propagation axis.

Electron Paramagnetic Resonance Spectroscopy. All low-temperature electron paramagnetic resonance (EPR) spectra (X-band, 9 GHz) were recorded on a Bruker EMX spectrometer equipped with an ER 4199HS cavity and an Oxford Instruments ESR900 continuous flow liquid helium cryostat outfitted with a Cernox sensor. EPR samples were prepared similarly as described above for the MCD experiments, but without the addition of glycerol. All samples were housed in 4-mm (outer diameter) quartz tubes and stored under liquid nitrogen.

Computational Methods. Initial atomic coordinates for Co^{2+}-bound site 1 and site 2 models were derived from X-ray crystallographic data (PDB IDs 4GGF for Mn^{2+}- and Ca^{2+}-bound hCP-Ser and 5W1F for Ni^{2+}- and Ca^{2+}-bound hCP-Ser).[11, 14] All models considered only the first coordination sphere (where the protein backbone atoms were removed and the α-carbon of each amino acid residue was converted to a methyl group) and were modified to add the appropriate number of hydrogen atoms, add or remove amino acid residues to model protein variants, and/or substitute the coordinated metal ion as appropriate. Density functional theory (DFT) geometry optimizations of these models were performed with the ORCA v. 2.9.0 or 2.9.1 software package.[46] All models contained a high-spin ($S = {}^{3}/_{2}$) Co^{2+} ion, for which Ahlrich's triple-ζ basis set with a polarization function (TZVP) was used.[47] The remaining atoms were modeled with the split-valence polarized (SVP) basis set.[48] All computations were carried out spin-unrestricted with Becke's three-parameter hybrid functional for exchange and the Lee-Yang-Parr functional for correlation (B3LYP).[49] Tight SCF convergence criteria were specified with an integration grid of 302 Lebedev points. The optimized models were used in subsequent single-point DFT computations with the same functional and basis sets as described above. To validate the computational results, time-dependent density functional theory (TDDFT) was used to calculate electronic transition energies and absorption intensities for each of the computational models. Absorption spectra were simulated by assuming that each transition gives rise to a Gaussian band with full width at half maximum of 1250 cm^{-1}, chosen based on spectral analyses of the experimental data. Electron density difference maps (EDDMs) for transitions of interest were generated with PyMOL using isodensity values of ±0.01 au.

Results and Discussion

Selection of CP variants and Sample Conditions. We elected to evaluate CP-Ser and an additional six variants in this study (Table 1) that include ΔHis_3Asp, ΔHis_4, ΔHis_3Asp D98A, ΔHis_3Asp H103A, ΔHis_3Asp H105A, and ΔHis_3Asp AHA (AHA indicates two amino acid substitutions, His103Ala and His105Ala). Excluding D98A, each of these variants has one or more amino acid residues that define the primary coordination sphere of site 1 (His_3Asp) or site 2 (His_6) substituted by non-coordinating Ala. The ΔHis_3Asp variant allows for Co^{2+} coordination by site 2 to be studied in isolation. Likewise, the variants composed of ΔHis_3Asp and one or more substitutions in the S100A9 C-terminal tail (D98A, H103A, H105A, AHA) allow for the contributions of the tail to be investigated in the absence of spectral contributions from the His_3Asp site. The ΔHis_4 variant has four His residues of site 2 replaced by Ala, which allows for site 1 to

10

be studied in isolation. All CP variants are based on CP-Ser, the S100A8(C42S)/S100A9(C3S) variant that has been extensively used in studies of metal-binding because the Cys→Ser substitutions allow studies to be done in the absence of a reductant.[19] This work focused on the spectroscopic characterization of the Co^{2+} sites of CP-Ser in the absence of Ca^{2+} ions.

Cobalt(II) Coordination at Site 2 (His_6 site). We first collected variable-temperature MCD spectra of Co^{2+}-bound CP-Ser, ΔHis_4, and ΔHis_3Asp (Figure 3). While the spectra obtained for CP-Ser and ΔHis_4 are nearly indistinguishable, they are markedly different form the spectra of ΔHis_3Asp (note that differences in MCD band intensities displayed by CP-Ser and ΔHis_4 are consistent with electronic absorption spectra reported previously[19] and may reflect a decreased Co^{2+} binding affinity of site 1 in the ΔHis_4 variant). The MCD spectra of Co^{2+}-bound ΔHis_3Asp display a pair of very weak negative features at 18,000 cm^{-1} and 20,500 cm^{-1} ($\Delta\varepsilon \approx 3\ M^{-1}cm^{-1}$). As mentioned above, MCD spectra of synthetic 6-coordinate Co^{2+} complexes invariably display a weak negative feature centered near 20,000 cm^{-1} with intensity and shape that vary depending on the degree of distortion from an ideal octahedral geometry and sometimes a second, very weak negative feature at slightly higher energy.[40, 42-44] Given the very low signal intensity observed here, the MCD spectra of the Co^{2+}-bound ΔHis_3Asp variant are consistent with an almost ideal octahedral coordination environment of the Co^{2+} ion in the His_6 site. This finding is in agreement with prior UV-Vis spectroscopic studies, which revealed that Co^{2+}-bound ΔHis_3Asp displays a very weak $d \rightarrow d$ transition centered at 20,040 cm^{-1} ($\varepsilon \approx 38\ M^{-1}cm^{-1}$), also characteristic of a centrosymmetric binding site.[19] It is therefore reasonable to conclude that Co^{2+} bound at site 2 of CP is coordinated by the His_6 motif defined by His17 and His27 of S100A8 and His91, His95, His103, and His105 of S100A9, as has previously been established for Mn^{2+}, Fe^{2+}, Ni^{2+} and Zn^{2+}.

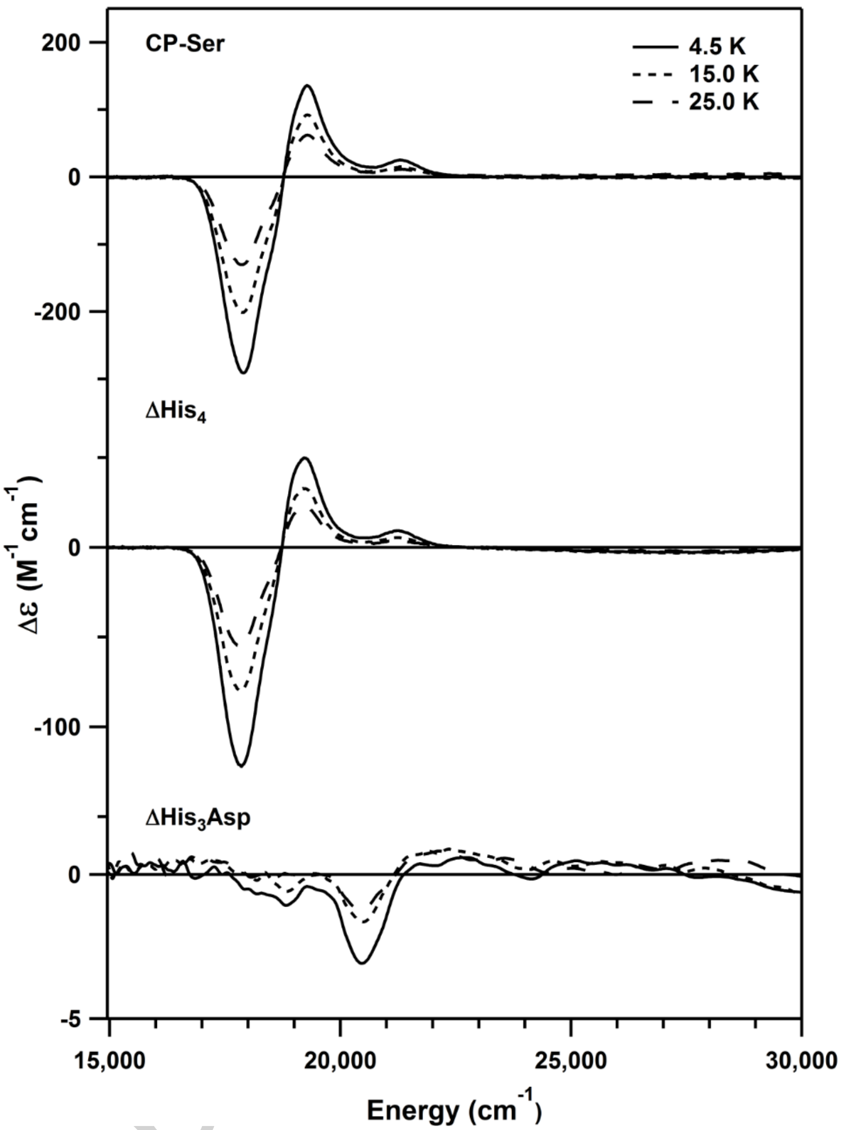

Figure 3. Variable temperature MCD spectra at 7 T of Co^{2+}-bound CP-Ser and the site variants ΔHis_4 and ΔHis_3Asp. Note that different y-axis scales are used for the different data sets. All protein sample concentrations were 1.0-1.1 mM *αβ* dimer in 75 mM HEPES buffer, pH 7.0-7.5, with 0.80-0.84 eq. Co^{2+} in 58-65% (v/v) glycerol.

To further probe Co^{2+} binding by site 2 and examine contributions from the S100A9 C-terminal tail residues, MCD spectra were collected for the Co^{2+}-bound D98A, H103A, H105A, and AHA (i.e., H103A/H105A) variants of ΔHis_3Asp (Figures 4 and S4).[19] The MCD spectra of the Co^{2+}-bound ΔHis_3Asp D98A variant are similar to, albeit slightly more intense than, those of Co^{2+}-bound ΔHis_3Asp, displaying a pair of negatively-signed features near 18,000 cm^{-1} and 20,500 cm^{-1} ($\Delta\varepsilon \approx 6$ $M^{-1}cm^{-1}$). By contrast, the MCD spectra of the Co^{2+}-bound ΔHis_3Asp H103A, H105A, and AHA variants display only a single negative feature near 20,500 cm^{-1} that is considerably more intense ($\Delta\varepsilon \approx 15$ $M^{-1}cm^{-1}$) than those of the D98A and ΔHis_3Asp variants. In early studies of Mn^{2+} binding, CP-Ser variants with these C-terminal tail amino acid substitutions were designed and studied biochemically and spectroscopically.[22] The CP-Ser D98A variant displayed comparable Mn^{2+} EPR spectral signatures and binding properties to CP-Ser, whereas substitution of His103 and/or His105 with Ala resulted in a loss of the EPR signal characteristic of Mn^{2+} bound to the His_6 site and lower Mn^{2+} binding affinities.[22] These results, along with crystallographic studies, demonstrated that His103 and His105 but not Asp98 bind Mn^{2+} at site 2. Similarly, our MCD spectra indicate that His103 and His105 also play an important role in Co^{2+} binding at site 2, and that substitution of Asp98 with Ala only weakly perturbs site 2.

13

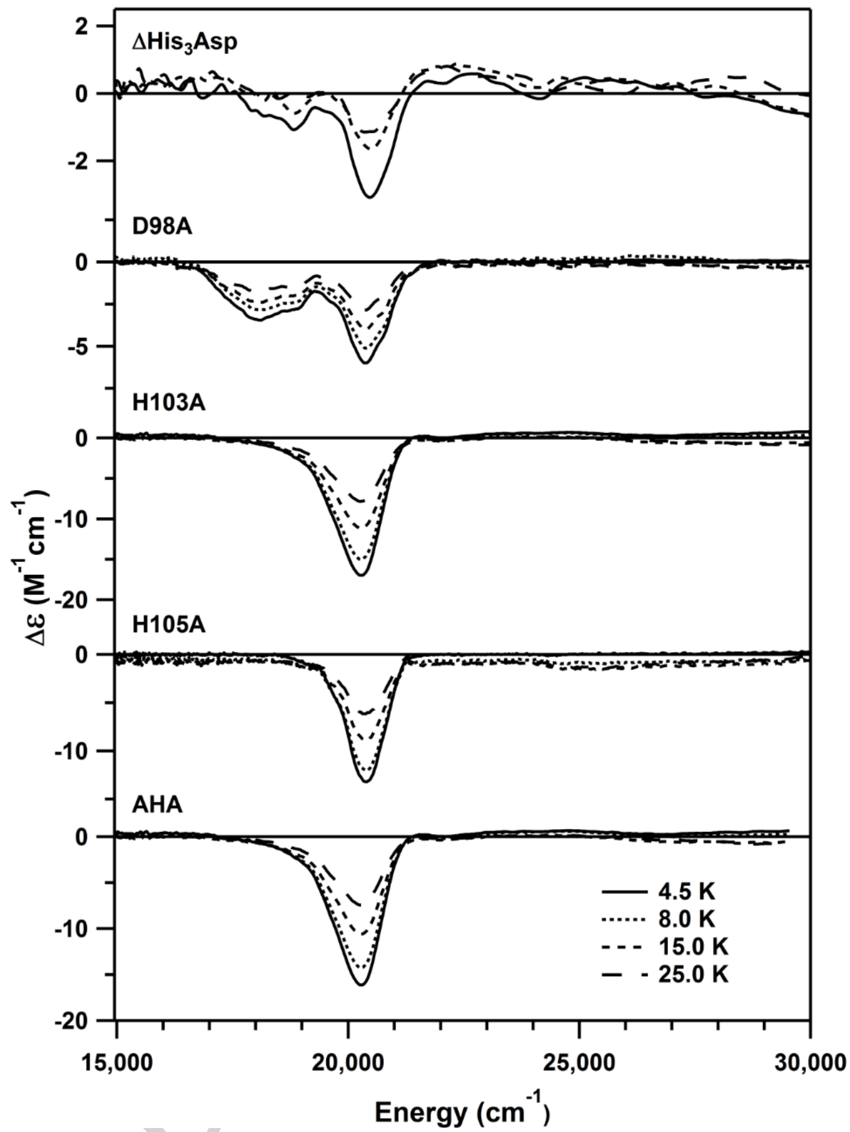

Figure 4. MCD spectra of Co^{2+}-bound ΔHis_3Asp C-terminal tail variants. Note that different y-axis scales are used for the different data sets. The protein concentrations were 1.0-1.1 mM *αβ* dimer in 75 mM HEPES buffer, 100 mM NaCl, pH 7.0-7.5. All samples contained 0.80-0.95 eq. Co^{2+} in 54-58% (v/v) glycerol.

As noted above, the spectral differences between Co^{2+}-bound ΔHis_3Asp and its D98A variant are small and primarily involve a minor increase in overall intensity observed for the latter. This difference may indicate a very slight perturbation to the symmetry about the Co^{2+} center, as is expected for the substitution of a non-ligating residue. Although the MCD signal intensities and

14

pattern of the D98A variant are strongly indicative of an intact His_6 site, the additional, negatively signed feature at lower energy (~ 18,000 cm^{-1}) could potentially arise from a small fraction of a 5-coordinate Co^{2+} species.[40, 41, 50] To investigate this possibility, the temperature dependence of the MCD data of the D98A variant was examined further, since features arising from different species should exhibit different saturation behavior due to differences in the zero-field splitting (ZFS) parameters.[51] We found that all features display similar temperature dependence (Figure S5), which suggests that a single Co^{2+} species contributes to the MCD spectrum of the D98A variant.

The MCD spectra of the ΔHis_3Asp H103A, H105A, and AHA variants are nearly identical (Figure 4). Each spectrum displays a single, negatively-signed feature centered at ~20,300 cm^{-1} as would be expected for octahedrally-coordinated Co^{2+} species, but these features are at least twice as intense as their counterparts in the spectra of ΔHis_3Asp and its D98A variant. This finding suggests that the 6-coordinate geometry is preserved in these variants; however, substitution of one or both ligating His103 and His105 residues eliminates the inversion symmetry. We reason that the octahedral Co^{2+} coordination sphere in these variants is completed by either solvent-derived water molecules or possibly other protein residues and favor the former possibility based on prior studies. Advanced EPR spectroscopic studies of Mn^{2+} bound to the His_6 site revealed that water molecules access the Mn^{2+} center when His103 and/or His105 are replaced by Ala.[12] Similarly, previous MCD spectroscopic studies of Fe^{2+}-bound H103A and H105A CP-Ser revealed that water-derived molecules coordinate to the Fe^{2+} center in these variants.[29]

We also collected low-temperature EPR spectra of Co^{2+}-bound ΔHis_3Asp D98A, H103A, H105A, and AHA and compared these spectra to previously reported spectra of Co^{2+}-bound ΔHis_3Asp and ΔHis_4 (Figure 5).[19] All spectra are characteristic of high-spin (S = 3/2) Co^{2+}

15

species with no observable ^{59}Co (I = 7/2) nuclear hyperfine structure. Consistent with the MCD spectra (Figure 4), the EPR spectra of ΔHis$_3$Asp and its D98A variant are nearly indistinguishable, whereas those obtained for the Co^{2+}-bound H103A, H105A, and AHA ΔHis$_3$Asp variants show a significant degree of perturbation (note that based on the signals in the g~5.5 region, a small fraction of a second species may be present in the samples of ΔHis$_3$Asp and its D98A variant). These results further support the involvement of (A9)H103 and (A9)H105 in Co^{2+} binding. Also consistent with the MCD spectra (Figure 4) is the close resemblance of the EPR spectra displayed by the Co^{2+}-bound H103A, H105A, and AHA ΔHis$_3$Asp variants, which further indicates that Ala substitution of H103, H105, or both has essentially the same effect on the Co^{2+} coordination environment in site 2.

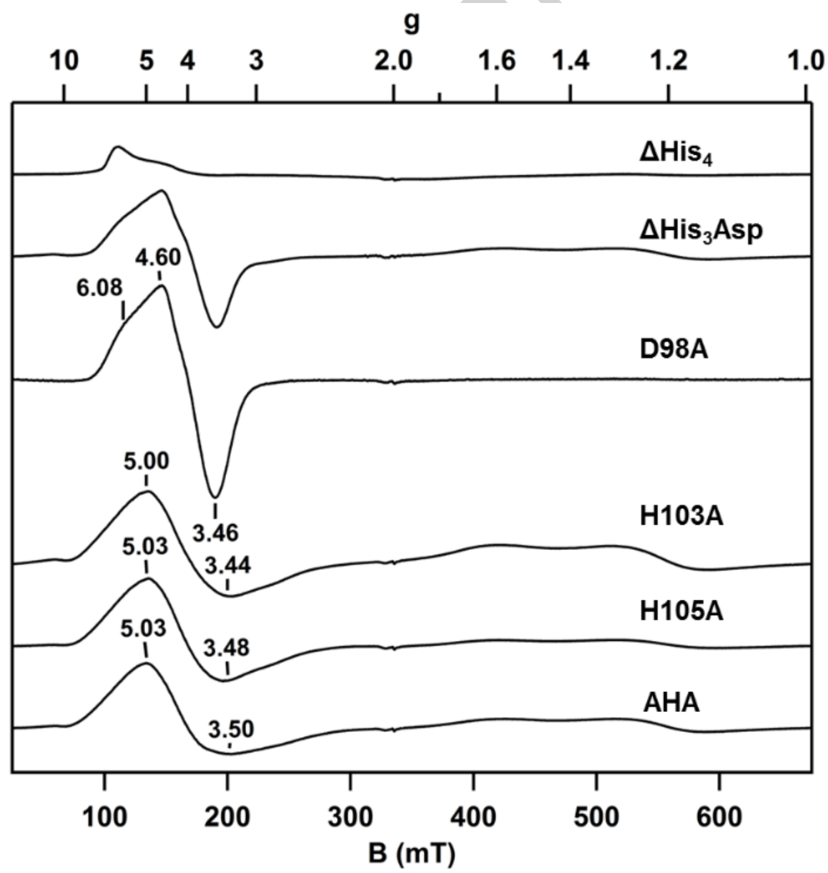

16

Figure 5. Low-temperature X band (9.4 GHz) EPR spectra at 10 K of Co^{2+}-bound ΔHis_4, ΔHis_3Asp, and the ΔHis_3Asp C-terminal tail variants. Protein sample concentrations were 1.0 mM $\alpha\beta$ dimer with 800 μM Co^{2+} at pH 7.0 (75 mM HEPES, 100 mM NaCl).

Next, computational methods were used to further explore the coordination environment of Co^{2+} bound to site 2. Models of this site were constructed based on the Mn^{2+}-bound crystal structure (PDB ID 4GGF[11]) with six neutral His residues, both with and without the potentially hydrogen-bonding second coordination sphere residues Asp65, Asp98, and the amide backbone of Ile13 (Figure S6). In general, models with one or more hydrogen-bonded His residue(s) converged to unreasonable geometries, with abstraction of protons from the His residues by the Asp65 and Asp98 residues. In addition, the His_6 models with hydrogen-bonding generally yielded TDDFT computed absorption spectra exhibiting charge-transfer transitions in the visible region that have no experimental counterparts.[19] In comparison, the first sphere only His_6 model based on the Mn^{2+}-bound structure yielded by far the most reasonable geometry (Figure 6A and Table S5, with key metric parameters included in Tables S6 and S7) and TDDFT-calculated transition energies and absorption intensities (Figure 7) when compared to the corresponding experimental data (Figure 8). Importantly, the absorption feature at ~20,000 cm^{-1} in the TDDFT-computed spectrum for the His_6 model aligns well with the weak absorption feature at 20,040 cm^{-1} in the experimental absorption spectrum.[19] Electron density difference maps (EDDMs) for the transitions in the visible region of the computed absorption spectrum, which provide a visual representation of the changes in electron density upon electronic excitation, indicate that all are Co^{2+} $d \rightarrow d$ transitions (Figure S7), as expected. The computed absorption intensities are slightly underestimated for this model, as expected because the TDDFT method ignores vibronic coupling (or Herzberg-Teller coupling), the mechanism by which symmetry-forbidden transitions gain electric dipole intensity.[52, 53]

17

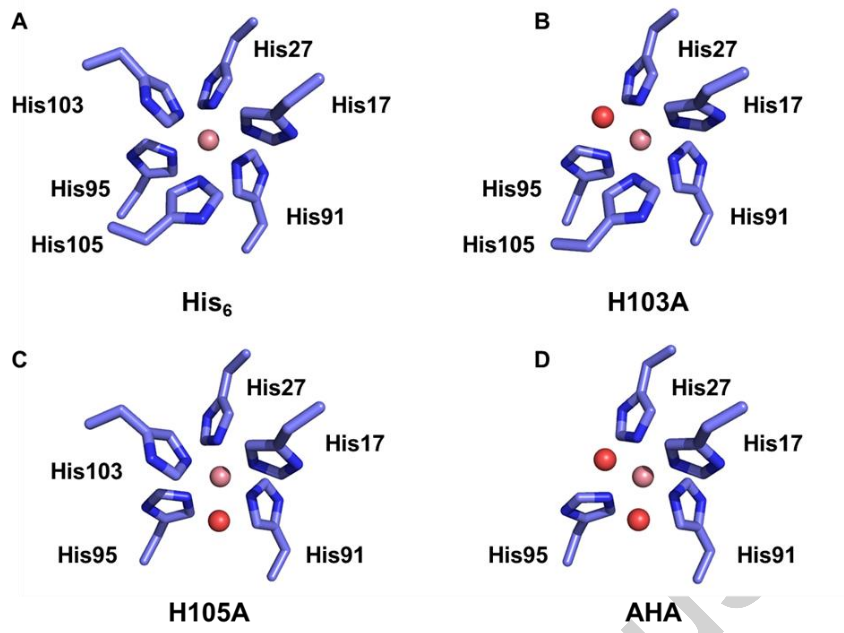

Figure 6. DFT optimized Co^{2+}-bound site 2 models. (A) CP-Ser His$_6$, (B) H103A, (C) H105A, and (D) AHA. Cobalt ions are represented by pink spheres, and solvent-derived water molecules are shown as red spheres. Hydrogen atoms have been omitted for clarity.

To further explore the Co^{2+}-binding sites of the H103A, H105A, and AHA ΔHis$_3$Asp variants, additional models were generated starting from the optimized His$_6$ site model by substituting one or two His residues with water molecules (Figure 6B-D). The relevant metric parameters for these models are included in Table S6, optimized coordinates are listed in Tables S8-S10, and the TDDFT-calculated absorption spectra are shown in Figure 7 (see Figures S8 and S9 for representative EDDMs). All three models converged to reasonable geometries, with the remaining average Co^{2+}–N(His) bond distances differing by less than 0.07 Å from those of the His$_6$ model. The TDDFT-computed absorption spectrum for the AHA variant model with two water molecules replacing His103 and His105 reproduces the experimental data for all three variants reasonably well (Figures 7 and 8), whereas the computed spectra for the H103A and H105A models featuring a single water molecule and five His residues exhibit multiple features

18

in the 15,000 – 28,500 cm^{-1} spectral region that have no counterparts in the experimental data (Figure 4). From these computations and the MCD and EPR spectroscopic data (Figures 4 and 5), we propose that the six-coordinate, distorted octahedral Co^{2+} coordination environments of the H103A and H105A ΔHis_3Asp variants are completed by four His residues and two water molecules. Hence, it appears that coordination of both His103 and His105 is required for the ordering of the S100A9 C-terminal tail in response to Co^{2+} binding to site 2. Interestingly, previous advanced EPR spectroscopic studies of Mn^{2+}-bound CP-Ser variants provided evidence that the number of exchangeable protons at site 2 increases from H105A to H103A and AHA ΔHis_3Asp [19], indicating that the presence of His103 or His105 alone is sufficient for the S100A9 C-terminal tail to coordinate to site 2-bound Mn^{2+}.

Lastly, we note that an examination of the crystal structures of apo- and Mn^{2+}-bound CP-Ser (PDB IDs 1XK4[13], 4GGF[11], and 4XJK[12]) reveals hydrogen-bonding interactions that may contribute to the high affinity of the His_6 site for Mn^{2+} as well as other metal ions that are coordinated in the same manner. In particular, extended hydrogen-bonding networks involving His95, Asp98, and His61 or His27, Asp65, and Arg85 could serve to induce partial, finely-tuned anionic character into the coordinating His residues, which would help balance the positive charge of the bound metal ion.[12, 22] A comparison of the X-ray crystal structures of apo CP-Ser and its Mn^{2+}-bound derivative reveals a large change in the positioning of the His27/Asp65 pair in response to Mn^{2+} binding, which may also contribute to the ordering of the S100A9 C-terminal tail (Figure S6). In the apo-CP structure (PDB ID 1XK4[13]), hydrogen-bonding interactions likely exist between His27, Asp65, and His61, and the repositioning of His27 and Asp65 in the Mn^{2+}-bound form allows His61 to interact with Asp98, which in turn hydrogen-bonds with the coordinating His95. These hydrogen bonding networks are also present in the X-ray crystal structure of Mn^{2+}- and Ca^{2+}-bound CP-Ser (PDB ID 4XJK[24]), and alignment of the apo- and Ni^{2+}-and Ca^{2+}-bound structures (PDB IDs 1XK4[13] and 5W1F[14]) reveals similar shifts in the positioning of second-sphere residues His61, Asp65, and the site 2 residue His27 upon Ni^{2+} binding. While it is possible that the movement of Asp98, the first residue in the C-terminal tail that becomes ordered upon coordination of Mn^{2+}, could trigger the ordering of the remaining C-terminal residues, neither the MCD (Figure 4) nor EPR (Figure 5) spectroscopic data obtained for Co^{2+}-bound ΔHis$_3$Asp and its D98A variant show any significant differences, which would be expected if this substitution precluded wrapping of the C-terminal tail entirely. Our results are consistent with previous studies of the D98A, H103A, H105A, and AHA ΔHis$_3$Asp variants, which also revealed that substitution of Asp98 did not appreciably affect the Mn^{2+} binding affinity of CP, while substitution of one or both of the His103 or His 105 residues had a significant impact.[22]

20

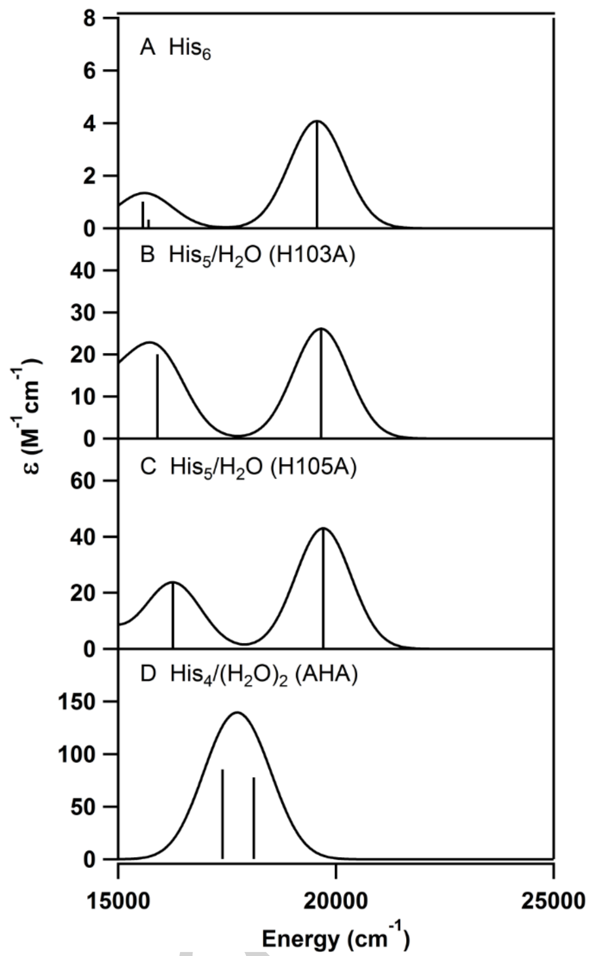

Figure 7. Comparison of TDDFT-calculated absorption spectra for Co^{2+}-bound site 2 models of CP-Ser. (A) His_6 model, (B) His_5/H_2O model with a water molecule replacing His103, (C) His_5/H_2O model with a water molecule replacing His105, and (D) $His_4/(H_2O)_2$ model with water molecules replacing both His103 and His105. Note that different y-axis scales are used for the different data sets.

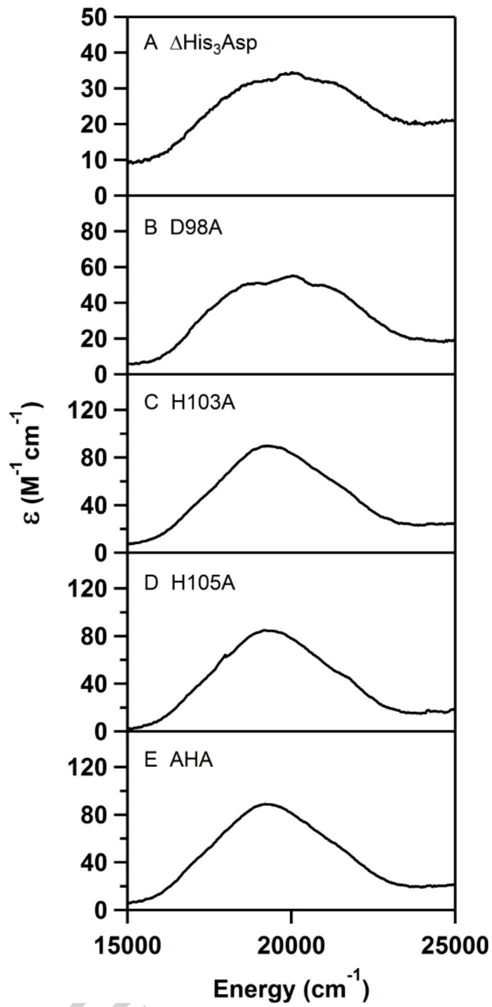

Figure 8. Comparison of experimental electronic absorption spectra of Co^{2+}-bound (A) ΔHis$_3$Asp, (B) D98A ΔHis3Asp, (C), H103A ΔHis3Asp, (D) H105A ΔHis3Asp, and (E) AHA ΔHis3Asp. Data shown are for final protein concentrations of 385 μM *αβ* dimer with 4 eq. Co^{2+}. Note that different y-axis scales are used for the different data sets. Co^{2+}-binding titration data for these species are shown in Figure S4.

In summary, this spectroscopic and computational analysis of Co^{2+} bound to site 2 of CP-Ser provides compelling evidence that the Co^{2+} ion is coordinated in a nearly idealized octahedral geometry by the His$_6$ motif defined by His17 and His27 of S100A8, and His91, His95, His103 and His105 of S100A9. To our knowledge, no other MCD spectra of highly symmetric octahedral Co^{2+}-bound metalloprotein species have been reported.

Cobalt(II) Coordination at Site 1 (His_3Asp site). The MCD spectra of Co^{2+}-bound CP-Ser and ΔHis_4 (Figure 3), both of which are dominated by site 1, exhibit an intense negative feature near 18,000 cm^{-1} ($\Delta\varepsilon \approx 150$–$300$ $M^{-1}cm^{-1}$ at 4.5 K) and a positive feature near 19,000 cm^{-1} ($\Delta\varepsilon \approx 100$ $M^{-1}cm^{-1}$). These features coincide with the relatively weak bands observed in the corresponding electronic absorption spectra (centered at 18,000 cm^{-1}, $\varepsilon \approx 280$ $M^{-1}cm^{-1}$ for ΔHis_4), which were previously assigned as ligand-field ($d \rightarrow d$) transitions of high-spin Co^{2+} ($S = 3/2$) centers.[19, 54] The pattern and intensities of the MCD features are characteristic of 4-coordinate, distorted tetrahedral Co^{2+} complexes.[40, 41, 44] For example, published electronic absorption and MCD spectra of Co^{2+}-substituted carbonic anhydrase, which contains a distorted tetrahedral His_3/H_2O coordination environment, display nearly identical features in this region.[55] Thus, our MCD data suggest monodentate Asp30 ligation of Co^{2+} at site 1 in solution. However, a 5-coordinate Co^{2+} species arising from bidentate Asp ligation could produce less intense features that might be obscured by the intense signal associated with the 4-coordinate species.[40, 41, 44] Hence, the presence of a minor 5-coordinate species with bidentate Asp coordination cannot be ruled out solely on the basis of our MCD data. We therefore performed an EPR power saturation study of Co^{2+}-bound ΔHis_4 at 5, 10, and 20 K (Figure S10) to explore whether the Co^{2+} ion might adopt more than a single coordination geometry at the His_3Asp site. Indeed, power saturation data obtained at 5 and 10 K show a weak signal at $g \sim 4.5$ that exhibits a different saturation behavior than the feature at $g > 6$. We therefore conclude that while the MCD spectra exhibited by Co^{2+}-bound CP-Ser and $\Delta His4$ (Figure 3) are dominated by a 4-coordinate species with monodentate Asp coordination, a small fraction of a second, potentially 5-coordinate species with bidentate Asp coordination at site 1 is present in these samples.

23

Prior structural studies of CP-Ser featuring Mn^{2+} or Ni^{2+} bound to the His_3Asp site revealed monodentate or bidentate Asp30 ligation depending on the identity of the bound metal ion and sample conditions. For instance, a crystal structure of Mn^{2+}- and Ca^{2+}-bound CP-Ser shows both 4- and 5-coordinate coordination environments of a metal ion modeled as Mn^{2+} at the His_3Asp site arising from monodentate and bidentate ligation of Asp30, respectively.[11] Alternatively, in the crystal structure of Ni^{2+}- and Ca^{2+}-bound CP-Ser, the Ni^{2+} ion only adopts a 4-coordinate geometry with monodentate Asp30 ligation at this site.[14] In the absence of Ca^{2+}, however, the Ni^{2+} ion resides in a 6-coordinate coordination environment completed by bidentate Asp30 ligation and a water molecule.[25] We also note that MCD spectroscopic studies of Fe^{2+}-bound wild-type and variant CP-Ser species indicated a 5-coordinate Fe^{2+} environment at the His_3Asp site but could not distinguish whether this resulted from monodentate Asp30 coordination and additional binding of a water molecule or bidentate Asp30 binding.[29]

To further assess the coordination mode of the Asp ligand at the His_3Asp site, DFT geometry optimizations were performed on two Co^{2+}-bound His_3Asp site models. The first model, based on the Ni^{2+}- and Ca^{2+}-bound X-ray crystal structure (PDB ID 5W1F[14]), features monodentate Asp30 ligation whereby the position of the non-ligating Asp30–O was frozen during geometry optimization (Figure 9A). The second model, based on the Mn^{2+}- and Ca^{2+}- bound structure (PDB ID 4GGF[11]), features bidentate Asp30 coordination (Figure 9B). The crystal structures used to extract the initial coordinates share nearly identical α-carbon positioning for the His_3Asp site residues. The optimized coordinates for these Co^{2+}-bound His_3Asp site models are listed in Tables S11 and S12, respectively, and relevant bond distances and angles are listed in Table S13. The Co–O(Asp) bond distances are consistent with monodentate Asp ligation in the monodentate model based on the Ni^{2+}-bound CP-Ser structure (1.91 Å and 3.22 Å) and bidentate, though

24

asymmetric, Asp ligation in the bidentate model based on the Mn^{2+}-bound structure (2.00 Å and 2.30 Å). To assess which model provides a better description of the Co^{2+}-bound His_3Asp site of CP-Ser, TDDFT was used to predict the electronic transition energies and absorption intensities for both models. A comparison of the TDDFT-computed (Figure 10) and experimentally derived (from a Gaussian deconvolution of the electronic absorption spectrum of Co^{2+}-bound ΔHis_4, see Figure 11) transition energies and intensities indicates that the experimental data are better reproduced with the monodentate Asp model (Table S14), for which three Co^{2+} $d \rightarrow d$ transitions with similar energies are correctly predicted (EDDMs for these transitions are shown in Figure S11). By contrast, for the bidentate model TDDFT predicts only two transitions with similar energies and a third transition at much lower energy (see Figure S12 for EDDMs). Collectively, our MCD and TDDFT results favor a 4-coordinate geometry for Co^{2+} bound at the His_3Asp site.

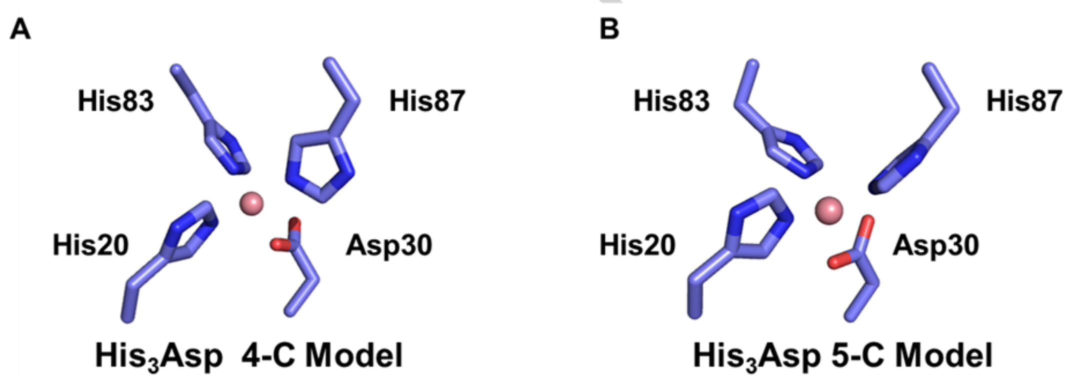

Figure 9. DFT-optimized Co^{2+}-bound site 1 models. (A) 4-coordinate (4-C) His_3Asp model and (B) 5-coordinate (5-C) His_3Asp model with monodentate and bidentate Asp30 ligation, respectively. Cobalt ions are represented by pink spheres, and solvent-derived water molecules are shown as red spheres. Hydrogen atoms have been omitted for clarity.

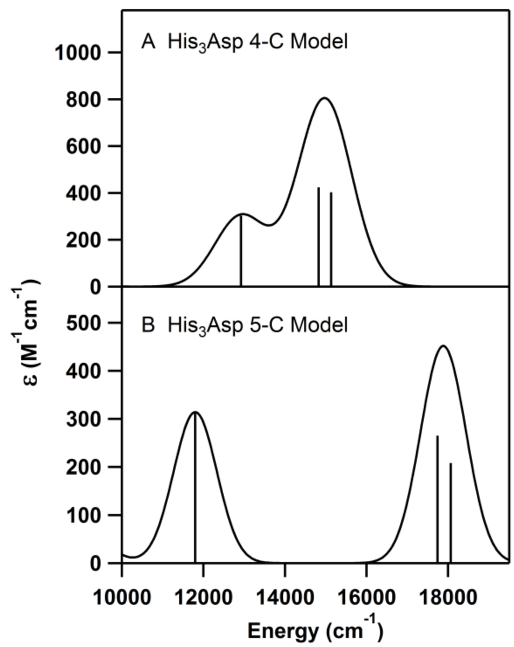

Figure 10. Comparison of TDDFT-calculated absorption spectra for Co^{2+}-bound site 1 models of CP-Ser. (A) 4-coordinate His_3Asp model with monodentate Asp30 ligation and (B) 5-coordinate His_3Asp model with bidentate Asp30 ligation. A bandwidth of 1250 cm^{-1}, as determined experimentally, was used to simulate these spectra. Note that different y-axis scales are used for the different data sets.

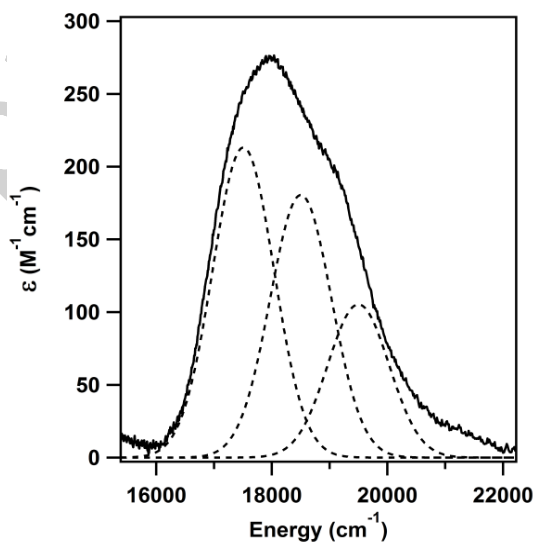

Figure 11. Gaussian deconvolution (with constant bandwidth of 1250 cm^{-1}) of the experimental room temperature absorption spectrum of Co^{2+}-bound ΔHis_4. Protein sample concentration was 1.0 mM in 75 mM HEPES buffer, pH 7.0, with 800 μM Co^{2+} in 59% (v/v) glycerol.

26

Conclusions

This spectroscopic and computational examination of Co^{2+}-bound CP-Ser and variants provides new information about the Co^{2+} coordination environment at the His_6 and His_3Asp sites. Overall, MCD and EPR spectroscopic data support nearly idealized octahedral coordination of Co^{2+} by the His_6 site. Moreover, MCD spectroscopic data in conjunction with computational results of CP-Ser and ΔHis_4 indicate that Co^{2+} bound to the His_3Asp site resides in a distorted tetrahedral coordination environment, indicating that Asp30 serves as a monodentate ligand to the Co^{2+} ion under the experimental conditions used in this work. These results further our fundamental understanding of the biological coordination chemistry of CP. Whether human CP coordinates Co^{2+} under any physiological or pathological conditions warrants exploration.

Acknowledgments. This work was supported by the National Science Foundation Grant No. CHE-1352132 (CAREER to EMN), the National Science Foundation Graduate Research Fellowship Program under Grant No. DGE-1256259 (fellowship to MMK), and the National Science Foundation grant CHE-0840494 (computational resources).

References

1 M. I. Hood and E. P. Skaar (2012) Nature Reviews Microbiology 10:525-537

2 L. D. Palmer and E. P. Skaar (2016) In: N. M. Bonini (ed) Annual review of genetics, vol 50. pp. 67-91

3 K. J. Waldron, J. C. Rutherford, D. Ford and N. J. Robinson (2009) Nature 460:823-830

4 C. C. Murdoch and E. P. Skaar (2022) Nature Reviews Microbiology 20:657-670

5 E. D. Weinberg (1975) Jama-Journal of the American Medical Association 231:39-41

27

6 E. M. Zygiel and E. M. Nolan (2018) In: R. D. Kornberg (ed) Annual review of biochemistry, vol 87. pp. 621-643

7 M. J. Hunter and W. J. Chazin (1998) Journal of Biological Chemistry 273:12427-12435

8 T. Vogl, J. Roth, C. Sorg, F. Hillenkamp and K. Strupat (1999) Journal of the American Society for Mass Spectrometry 10:1124-1130

9 N. Leukert, T. Vogl, K. Strupat, R. Reichelt, C. Sorg and J. Roth (2006) Journal of Molecular Biology 359:961-972

10 K. Strupat, H. Rogniaux, A. Van Dorsselaer, J. Roth and T. Vogl (2000) Journal of the American Society for Mass Spectrometry 11:780-788

11 S. M. Damo, T. E. Kehl-Fie, N. Sugitani, M. E. Holt, S. Rathi, W. J. Murphy, Y. F. Zhang, C. Betz, L. Hench, G. Fritz, E. P. Skaar and W. J. Chazin (2013) Proceedings of the National Academy of Sciences of the United States of America 110:3841-3846

12 D. M. Gagnon, M. B. Brophy, S. E. J. Bowman, T. A. Stich, C. L. Drennan, D. R. Britt and E. M. Nolan (2015) JACS 137:3004-3016

13 I. P. Korndorfer, F. Brueckner and A. Skerra (2007) Journal of Molecular Biology 370:887-898

14 T. G. Nakashige, E. M. Zygiel, C. L. Drennan and E. M. Nolan (2017) Journal of the American Chemical Society 139:8828-8836

15 T. G. Nakashige, J. R. Stephan, L. S. Cunden, M. B. Brophy, A. J. Wommack, B. C. Keegan, J. M. Shearer and E. M. Nolan (2016) Journal of the American Chemical Society 138:12243-12251

16 T. G. Nakashige, B. Zhang, C. Krebs and E. M. Nolan (2015) Nature Chemical Biology 11:765-+

17 J. Adhikari, J. R. Stephan, D. L. Rempel, E. M. Nolan and M. L. Gross (2020) Journal of the American Chemical Society 142:13372-13383

18 R. Silvers, J. R. Stephan, R. G. Griffin and E. M. Nolan (2021) Journal of the American Chemical Society 143:18073-18090

19 M. B. Brophy, J. A. Hayden and E. M. Nolan (2012) Journal of the American Chemical Society 134:18089-18100

28

20 J. A. Hayden, M. B. Brophy, L. S. Cunden and E. M. Nolan (2013) Journal of the American Chemical Society 135:775-787

21 J. R. Stephan and E. M. Nolan (2016) Chemical Science 7:1962-1975

22 M. Brophy, T. Nakashige, A. Gaillard and E. Nolan (2013) Journal of the American Chemical Society 135:17804-17817

23 T. G. Nakashige and E. M. Nolan (2017) Metallomics 9:1086-1095

24 D. M. Gagnon, M. B. Brophy, S. E. J. Bowman, T. A. Stich, C. L. Drennan, R. D. Britt and E. M. Nolan (2015) Journal of the American Chemical Society 137:3004-3016

25 T. G. Nakashige, S. E. J. Bowman, E. M. Zygiel, C. L. Drennan and E. M. Nolan (2018) Biochemistry

26 O. V. Moroz, E. V. Blagova, A. J. Wilkinson, K. S. Wilson and I. B. Bronstein (2009) Journal of Molecular Biology 391:536-551

27 D. E. Brodersen, J. Nyborg and M. Kjeldgaard (1999) Biochemistry 38:1695-1704

28 O. V. Moroz, A. A. Antson, S. J. Grist, N. J. Maitland, G. G. Dodson, K. S. Wilson, E. Lukanidin and I. B. Bronstein (2003) Acta Crystallographica Section D-Biological Crystallography 59:859-867

29 T. M. Baker, T. G. Nakashige, E. M. Nolan and M. L. Neidig (2017) Chemical Science 8:1369-1377

30 A. N. Besold, B. A. Gilston, J. N. Radin, C. Ramsoomair, E. M. Culbertson, C. X. Li, B. P. Cormack, W. J. Chazin, T. E. Kehl-Fie and V. C. Culotta (2018) Infection and Immunity 86

31 J. F. Wang, Z. R. Lonergan, G. Gonzalez-Gutierrez, B. L. Nairn, C. N. Maxwell, Y. X. Zhang, C. Andreini, J. A. Karty, W. J. Chazin, J. C. Trinidad, E. P. Skaar and D. P. Giedroc (2019) Cell Chemical Biology 26:745-+

32 E. M. Zygiel, C. E. Nelson, L. K. Brewer, A. G. Oglesby-Sherrouse and E. M. Nolan (2019) Journal of Biological Chemistry 294:3549-3562

33 W. Maret and B. L. Vallee (1993) Metallobiochemistry, Part C 226:52-71

29

34 B. L. Vallee (1971) In: W. Mertz and W. E. Cornatzer (eds) Newer trace elements in nutrition. Dekker, New York, pp. 33

35 B. L. Vallee, J. A. Rupley, T. L. Coombs and H. Neurath (1958) Journal of the American Chemical Society 80

36 B. L. Vallee (1973) Advances in experimental medicine and biology 40:1-12

37 M. M. Harding, M. W. Nowicki and M. D. Walkinshaw (2010) Crystallography Reviews 16:247-302

38 M. K. Johnson (2000) In: L. Que (ed) Physical methods in bioinorganic chemistry. University Science Books, Sausalito, CA, pp. 233-285

39 E. I. Solomon and A. B. P. Lever (1999) Inorganic electronic structure and spectroscopy. Wiley, New York

40 T. A. Kaden, Holmquis.B and B. L. Vallee (1974) Inorganic Chemistry 13:2585-2590

41 B. Holmquist, T. A. Kaden and B. L. Vallee (1975) Biochemistry 14:1454-1461

42 Z. Tomkowicz, S. Ostrovsky, S. Foro, V. Calvo-Perez and W. Haase (2012) Inorganic Chemistry 51:6046-6055

43 M. J. Harding and B. Briat (1973) Molecular Physics 25:745-776

44 J. A. Larrabee, G. Schenk, N. Mitic and M. J. Riley (2015) European Biophysics Journal with Biophysics Letters 44:393-415

45 M. B. Brophy, T. G. Nakashige, A. Gaillard and E. M. Nolan (2013) Journal of the American Chemical Society 135:17804-17817

46 F. Neese (2012) Orca. pp. An ab initio, DFT and semiempirical SCF-MO package

47 A. Schafer, C. Huber and R. Ahlrichs (1994) Journal of Chemical Physics 100:5829-5835

48 A. Schafer, H. Horn and R. Ahlrichs (1992) Journal of Chemical Physics 97:2571-2577

49 C. T. Lee, W. T. Yang and R. G. Parr (1988) Physical Review B 37:785-789

50 T. A. Kaden, B. L. Vallee and Holmquis.B (1972) Biochemical and Biophysical Research Communications 46:1654-&

30

51 E. I. Solomon, M. L. Neidig and G. Schenk (2004).

52 F. Neese (2006) Journal of Biological Inorganic Chemistry 11:702-711

53 F. Neese (2009) Coordination Chemistry Reviews 253:526-563

54 J. Krzystek, S. A. Zvyagin, A. Ozarowski, A. T. Fiedler, T. C. Brunold and J. Telser (2004) Journal of the American Chemical Society 126:2148-2155

55 J. A. Larrabee, C. M. Alessi, E. T. Asiedu, J. O. Cook, K. R. Hoerning, L. J. Klingler, G. S. Okin, S. G. Santee and T. L. Volkert (1997) Journal of the American Chemical Society 119:4182-4196

Graphic Abstract

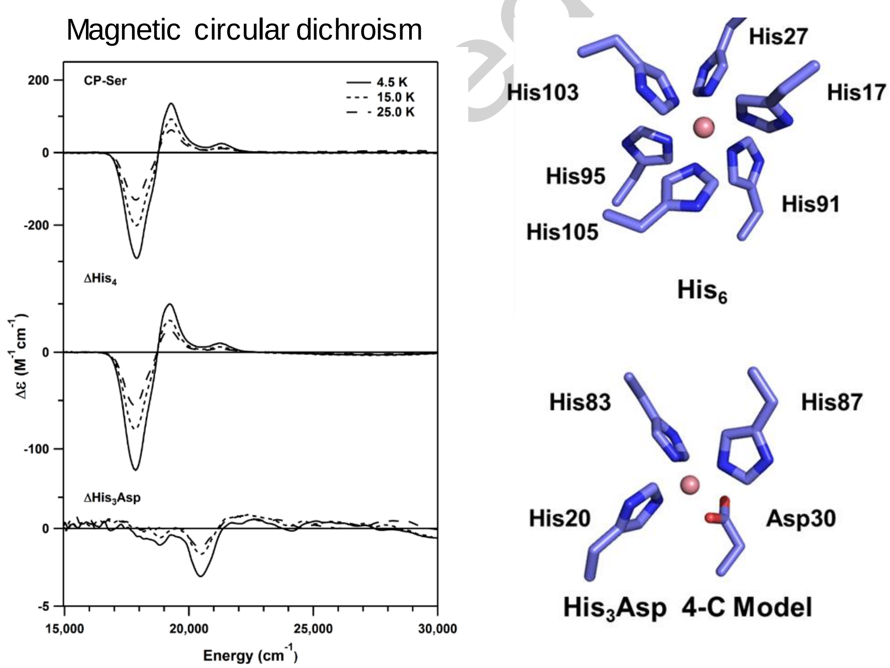

31